Natural stiffening increases flaw tolerance of biological fibers

Tristan Giesa,[1] Nicola M. Pugno,[2] and Markus J. Buehler[1,3,*]

[1]*Laboratory for Atomistic and Molecular Mechanics, Department of Civil and Environmental Engineering, Massachusetts Institute of Technology, 77 Massachusetts Avenue, Room 1-235A&B, Cambridge, Massachusetts 02139, USA*

[2]*Laboratory of Bio-Inspired Nanomechanics, Department of Structural, Geotechnical and Building Engineering, Politecnico di Torino, Corsa Duca degli Abruzzi 24, 10129 Torino, Italy*

[3]*Center for Computational Engineering, Massachusetts Institute of Technology, 77 Massachusetts Avenue, Room 1-235A&B, Cambridge, Massachusetts 02139, USA*

(Received 28 February 2012; revised manuscript received 17 June 2012; published 8 October 2012)

Many fibers in biomaterials such as tendon, elastin, or silk feature a nonlinear stiffening behavior of the stress-strain relationship, where the rigidity of the material increases severely as the material is being stretched. Here we show that such nonlinear stiffening is beneficial for a fiber's ability to withstand cracks, leading to a flaw tolerant state in which stress concentrations around cracks are diminished. Our findings, established by molecular mechanics and the derivation of a theoretical scaling law, explain experimentally observed fiber sizes in a range of biomaterials and point to the importance of nonlinear stiffening to enhance their fracture properties. Our study suggests that nonlinear stiffening provides a mechanism by which nanoscale mechanical properties can be scaled up, providing a means towards bioinspired fibrous material and structural design.

DOI: 10.1103/PhysRevE.86.041902 PACS number(s): 87.19.R−, 81.05.Lg, 62.20.mm, 62.25.−g

I. INTRODUCTION

Biomaterials such as collagen, silk, elastin, or spectrin feature complex hierarchical architectures that are critical for their ability to achieve high strength and toughness [1]. Notably, they are often based on fibrous structures that display a nonlinear stiffening constitutive material behavior, where the stiffness increases severely as the material is being stretched. In many cases the nonlinear stiffening has been shown to result from entropic effects in protein molecules, which unfold and successively align and stiffen [2–7]. In this study, by means of a scaling law, we connect the universal nonlinear stiffening material behavior seen in a very broad class of fibrous biomaterials to their intrinsic fracture properties.

The concept of size effects in damaged materials, i.e., the scaling of fracture strength, dates back to Griffith's work in the 1920s, and since then has been thoroughly studied for metals, ceramics, and many other materials [8–11]. In flawed materials, e.g., a fiber with a preexisting crack, the strength is reduced due to stress concentrations that develop around defects, which compromise the mechanical integrity as they induce the propagation of fractures. Classical theory predicts that the strength of the crack-free material can only be reached by confining its dimension to a "critical size," here denoted by H^* [12,13]. When a flawed material is confined to H^*, it exhibits no stress concentration at the tip of a crack and reaches a homogeneous deformation state, indicating flaw tolerance.

For many materials including graphene and nanotubes the critical size tends to be close to the size of the atomic spacing (or the unit cell of a crystal) [14], suggesting that the flaw tolerant state is very difficult to achieve. Recent work showed that the critical size additionally depends on boundary conditions and other material properties [15–17]. The flaw tolerance mechanism has been experimentally confirmed for thin steel sheets and for notched nanoscale thin films, where no stress concentration could be observed and failure initiated far away from the crack tip [18,19].

Here, we hypothesize that the nonlinear stiffening behavior, i.e., the increasing elastic modulus during deformation as universally observed in many biological fibers, contributes to an increase of the critical size and therefore allowing them to perform well in spite of the presence of cracks (the larger the critical size, the larger the fiber diameter can be and still feature a flaw tolerant behavior). In order to gain insight into this mechanism, we use a simple bead-spring model with a power-law potential to systematically model stiffening and softening constitutive material behaviors (Sec. II). We then determine the critical size H^* at which the fiber performs as if it were unflawed (Sec. III). Additionally, we use nonlinear fracture mechanics to derive a scaling law that predicts the dependence of the critical size on the magnitude of the stiffening (Sec. IV). In Sec. V we use the results of the general study (Secs. II–IV) to determine the critical size for a set of materials with simple constitutive behaviors and show that fibrous biomaterials with stronger stiffening behavior often display larger fibril diameters. We conclude that a stiffening behavior may be advantageous for the fracture resistance of fibers.

II. COARSE-GRAINED FIBER MODEL AND PARAMETERS

In this section, we introduce the computational model used to determine the critical size of the fibers with varying material properties. Coarse-grained bead-spring models (also called the internal bond method) provide a simple but appropriate description of materials under axial tension [20,21], and have been successfully applied to predict various size effects [17,22–24]. This modeling technique applies to all systems where a characteristic size can be identified (the microstructure of the material) [21]. In this study, we set up a thin film with a face centered cubic lattice consisting of two unit cells in the out-of-plane direction [Fig. 1(a)]. A power-law

*Corresponding author: mbuehler@mit.edu

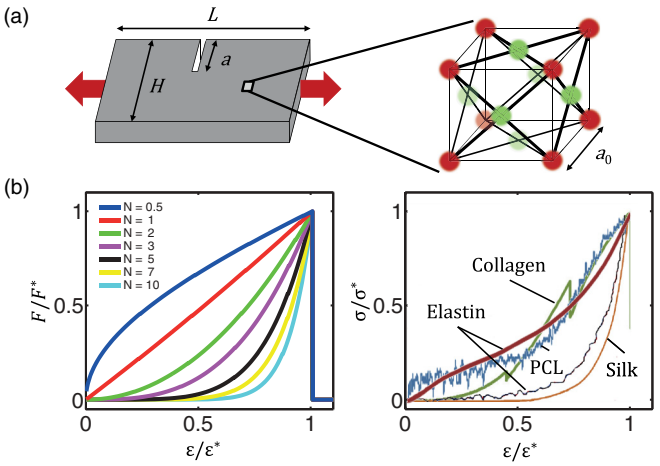

FIG. 1. (Color online) Geometry of the plane strain fiber model and constitutive behavior. (a) The fiber with length L, width H, and crack size a consists of a face centered cubic lattice with nearest neighbor interactions only. The fiber length is much larger than the width. The model contains two periodic layers of beads in the out-of-plane direction to enforce plane strain boundary conditions. The fiber is subjected to uniaxial tension. (b) The bond behavior for uniaxial tension is described by a nonlinear potential with controlling parameter N, a constant failure force $F^* = k_0 = 2.5$ kcal/(mol Å) and failure strain of $\varepsilon^* = 5\%$. Note that the actual values are irrelevant as this study is of comparative quality for the parameter N. The upper line refers to the lowest value of N studied here and the lower line to the highest value of N. During the computational experiments the width H is varied while keeping L, $\zeta = a/H$, and N constant. The simulations are motivated by experimental tensile stress-strain curves for, e.g., collagen (green [upper] line, $\sigma^* \approx 60$ MPa, $\varepsilon^* \approx 12\%$) [53]; polycaprolactone (PCL) microfibers (blue [upper] line, $\sigma^* \approx 25$ MPa, $\varepsilon^* \approx 4\%$) [5]; tropoelastin molecules (black [lower] line, $\sigma^* \approx 5$ MPa, $\varepsilon^* \approx 800\%$) [51]; elastin fibers (red [upper] line, $\sigma^* \approx 1.3$ MPa, $\varepsilon^* \approx 190\%$) [54]; and viscid silk (orange [lower] line, $\sigma^* \approx 450$ MPa, $\varepsilon^* \approx 3\%$) [2].

potential for the bonds with controlling parameter N serves as a model for the constitutive behavior of axially loaded fibers [Fig. 1(b)]. Under plane strain conditions this structure has properties similar to those of a cracked fiber with diameter H [25] (the characteristic dimension H typically denotes the fiber's diameter). Earlier studies suggested that it is adequate to model composite fibers with a power-law material constitutive behavior in plane strain [26–28].

In order to set up the molecular mechanics model, we define a potential between the particles that captures the physics of this problem and has a minimum number of parameters. A general description of a bond force-extension power law that comprises stiffening, softening, and linear behavior is given by

$$F(r) = k_0 \left[\frac{\varepsilon(r)}{\varepsilon^*}\right]^N, \tag{1}$$

where k_0 is the force at which the bond fails, $\varepsilon(r) = (r - r_0)/r_0$ with r_0 as equilibrium bond distance, ε^* is the failure strain of the bond, and $N > 0$ is a stiffening parameter. Bond force and bond potential are related by $F(r) = -F_{\text{bond}} = \partial\Phi/\partial r$ (tension). Hence, the pair potential between particles is

$$\Phi(r) = \frac{k_0 r_0 \varepsilon^*}{(N+1)} \left[\frac{\varepsilon(r)}{\varepsilon^*}\right]^{N+1}. \tag{2}$$

Because we normalize the critical size by the equilibrium bond distance r_0, the choice of k_0 and ε^* are somewhat arbitrary and the results maintain maximum generality. Furthermore, ε^* is not a controlling parameter of the solution [see Eq. (10) in Sec. IV] and $k_0 \sim \sigma^*$. For further details and discussion, see Secs. IV and V.

The parameter N controls the nature of the stress-strain behavior, including softening ($N < 1$), linear elasticity ($N = 1$), and stiffening ($N > 1$). For $N \in [0.5,1.0,2.0,3.0,5.0,7.0,10.0]$ the bond behaviors are shown in Fig. 1(b) with $F^* = k_0$, such that all constitutive behaviors studied vary only in their shape and lead to the same maximum attainable force (respectively, maximum stress σ^* in the lattice) and strain at the breaking point ε^*. All simulations are carried out using a conjugate gradient energy minimization approach implemented in the molecular simulation package LAMMPS [29].

The coarse-grained simulation parameters are chosen as reasonable values for the microstructure of many fibrous biomaterials, where $r_0 = 10$ nm (reflecting the characteristic size of structural domains), $k_0 = 2.5$ kcal/(mol Å), and $\varepsilon^* = 5\%$ [30,31]. Each specimen has an out-of-plane thickness of two unit cells, a length of 100 unit cells, and a width H that is varied to examine size effects. A surface crack of initial size a is introduced in the middle of the slab by deleting the bonds along the crack surface [Fig. 1(a)]. An out-of-plane periodicity enforces plane strain boundary conditions. The slab is axially strained with strain increments of 0.3%. Energy minimization is applied after each increment and convergence is ensured. The maximum stress σ^* can be calculated for the cubic lattice under plane strain by [32,33] as

$$\sigma^* = \frac{4r_0^2 k\varepsilon^*}{3\Omega_0} = \frac{4r_0 k_0}{3\Omega_0} = \frac{8k_0}{3\sqrt{2}r_0^2}, \tag{3}$$

where $k = k_0/(r_0\varepsilon^*)$ is the bond stiffness and Ω_0 is the volume of a bead in the unit cell, for the present crystal given by $\Omega_0 = a_0^3/4 = (\sqrt{2}r_0)^3/4$ (where a_0 is the lattice spacing; in a cubic crystal $a_0 = \sqrt{2}r_0$).

III. COARSE-GRAINED SIMULATION RESULTS

We perform a computational study to assess the effect of the constitutive law on flaw tolerance. We record the tensile failure stress and strain for the specimen with dimensions $L \times H \times t$ and crack size a. H is varied from $2a_0 = 28$ nm up to $50a_0 = 700$ nm. The dimension L is kept constant at $100a_0 = 1410$ nm and t is $2a_0 = 28$ nm. The tensile failure stress, calculated by the virial stress, is normalized by the failure stress of the perfect crystal unit cell σ^*. The critical size H^*, reflecting flaw tolerance in a homogeneous deformation state, is determined for varied material parameters N and crack size ratios $\zeta = a/H \in [0.075,0.15,0.25,0.5]$ by fitting the failure stress of a slab with fiber-like geometries ($H \ll L = 1.5$ μm) for varying H. We perform a linear regression in the stress-$1/\sqrt{H}$ plot [Fig. 2(a)]. We base this

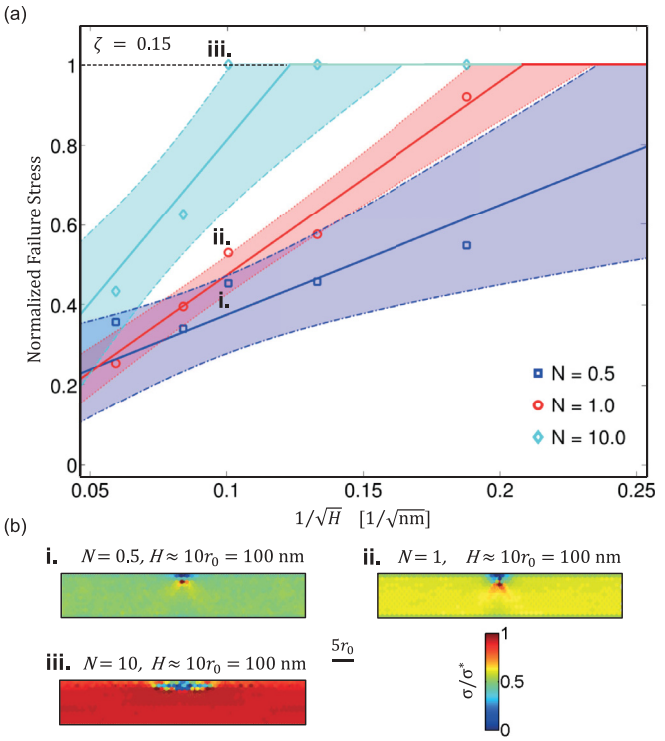

FIG. 2. (Color online) Normalized tensile failure stress versus inverse square root of the fiber width for $\zeta = a/H = 0.15$ and $N = 0.5$, 1.0, 10.0 and stress contour plots. (a) By decreasing the width (corresponding to the diameter) in the plane strain fiber model, the maximum attainable stress increases. For $N = 0.5$ and $N = 1.0$ classical fracture theory approximately predicts the size effects in the fiber (increasing failure stress versus decreasing diameter, full lines indicate linear fit and dotted lines indicate the $\alpha = 0.1$ confidence upper and lower bound for the linear regression). For $N = 10.0$ classical fracture theory breaks down at $H = 10r_0 \approx 100$ nm as the theoretical stress of the perfect crystal is reached. (b) Stress contour plots for $N = 0.5$ (i.), $N = 1.0$ (ii.), and $N = 10.0$ (iii.) indicate the reason for the observed behavior (same fiber diameter in all cases depicted). For $H \approx 100$ nm an enhanced delocalization of stress away from the crack tip can be observed for increasing N. The stress becomes almost perfectly homogeneous within the fiber (iii.) and thus the fiber reaches the failure stress of the perfect crystal despite the presence of a crack. These results confirm that by changing the nature of the nonlinear behavior of the material, at constant size, a flaw tolerant state can be achieved.

on the assumption that the strength scales approximately with $1/\sqrt{H}$, which reflects a prediction from linear elastic fracture mechanics. This assumption also holds true in our analysis, as discussed in Sec. IV. The classical scaling breaks down when the failure stress reaches the maximum attainable stress σ^*, as seen in Fig. 2(a).

An example of the analysis procedure used to determine the critical size is shown in Fig. 2(a) for $\zeta = 0.15$ and $N = 0.5, 1.0, 10.0$. Upper and lower bounds are shown for the linear regression for a confidence of $\alpha = 0.1$. Despite the crack, the failure stress approximately reaches the theoretical limit for $H = H^* \approx 6r_0 \approx 60$ nm and $N = 10.0$. The stress contour plots (for a constant fiber diameter $H \approx 100$ nm) depicted in Fig. 2(b) ($N = 0.5$ in i., $N = 1.0$ in ii., and $N = 10.0$ in iii.) directly confirm how the increase of the stiffening parameter N leads to a pronounced delocalization of the stress away from the crack tip, and eventually to a homogeneous deformation state. Notably, these results confirm that by changing the nonlinear behavior of the material (at constant size), a flaw tolerant state can be achieved.

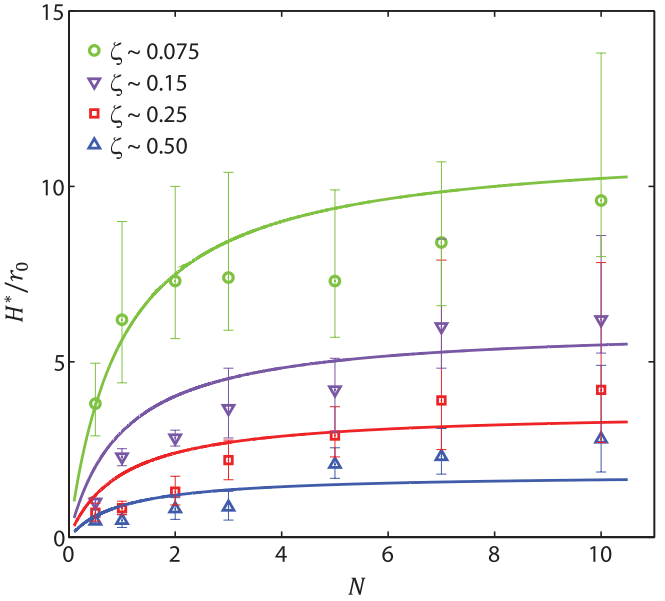

FIG. 3. (Color online) Comparison of simulation and analytical model predictions for the normalized critical size H^*/r_0 as a function of the material parameter N for varying crack dimensions $\zeta = a/H$. The critical size H^* increases with increasing stiffening behavior controlled by the parameter N. Smaller crack ratios ζ lead to an increasing critical size. The data show average values and their variance due to linear regression (see Fig. 2). A comparison of the simulation to the fracture mechanics prediction for $\tau = r_0$ nm show fairly good agreement and confirm a scaling law of the critical size $H^* \sim 1/(1 + 1/N)$. For increasing N the flaw tolerant behavior is reached at multiples of the characteristic system size, denoting a mechanism to upscale the perfect lattice behavior to significantly larger scales.

Additional results for H^* for various crack size ratios ζ and stiffness parameters N are shown in Fig. 3, including mean values as well as error bars for the variance from linear regression. Here, we normalize H^* by the characteristic size of the system r_0, a procedure that becomes clear in view of the discussion reported in Sec. IV. It can be seen that increasing N leads to larger critical sizes H^*, significantly exceeding the length scale parameter of the crystal r_0 (in our simulations that is 10 nm). We observe a saturation for the critical size H^* that is especially pronounced at smaller crack size ratios ζ. This indicates that a stronger stiffening does lead to larger critical sizes rendering fibers more resistant to flaws and damage.

IV. FRACTURE MECHANICS ANALYSIS

We derive a scaling law to confirm the dependence of increasing flaw tolerance length scales with increasing stiffening from fracture mechanics. We start our analysis of

the model from the small-scale yielding solution of the plane strain deformation of a material with nonlinear power-law constitutive behavior [26]. For the isotropic crystal the stress field singularity is on the order of the linear elastic solution supporting the strength scaling analysis in Sec. III [27]. For the given boundary conditions, the critical energy release rate is equal to the solution of the J integral,

$$J = G_c = \frac{\sigma^2 \pi a F^2(\zeta)}{E'}, \tag{4}$$

where σ is the far-field stress, a is the crack size, $\zeta = a/H$ with H as the width (respectively the diameter), and $F(\zeta)$ is a geometry dependent function [25]. For a nonlinear (elastic) material behavior the existence of the critical energy release rate is ensured, and in the case that $\sigma = \sigma^*$ where σ^* is the failure stress of the perfect crystal reached at $H = H^*$, this can be rewritten as

$$H^* = \frac{2\gamma_s E'}{\pi \zeta Q \sigma^{*2}}, \tag{5}$$

where E' is the equivalent Young's modulus and Q is a factor that includes $F(\zeta)$, as well as other geometric and material nonlinearities accounting for the fact that the stress field in a confined specimen is probably not J dominated. We are primarily interested in the general scaling behavior of the strength in such materials, and not in the details of the stress field. We determine γ_s, the surface energy set free during crack propagation, from the molecular mechanics setup according to [33]

$$\gamma_s(N) = \frac{\Delta\Phi(N)}{2dt} = \frac{4\Delta\Phi(N)}{r_0^2}. \tag{6}$$

The parameter $t = 2a_0 = 2\sqrt{2}r_0$ is the slab thickness and $d = r_0/(8\sqrt{2})$ is the average distance that the crack propagates in the model per broken bond while dissipating the energy $\Delta\Phi$ with

$$\Delta\Phi(N) = \int_0^{r^*} F(r)dr = \frac{k_0 r_0 \varepsilon^*}{N+1}. \tag{7}$$

When the homogeneous deformation state is reached, the material at the crack tip features the equivalent Young's modulus of cubic lattices under plane strain,

$$E'(N) = \frac{E_{fcc}(N)(1-\nu)}{1-\nu-2\nu^2}, \tag{8}$$

with [33]

$$E_{fcc}(N) = \frac{4(a_0/2)^4}{(a_0/\sqrt{2})^2}\frac{\partial^2\Phi/\partial r^2}{\Omega_0} = \frac{16k_0}{\sqrt{2}^3 r_0^2 \varepsilon^*}N. \tag{9}$$

The evaluation of $E'(N)$ and $\gamma_s(N)$ at $\varepsilon = \varepsilon^*$ is motivated by the fact that localized failure is controlled by the asymptotic bond behavior at the crack tip reaching the failure strain ε^*, which spreads over the entire fiber in the limit of the flaw tolerant state.

Combining Eqs. (3), (5), (6), and (8) yields

$$H^* = \frac{9}{\sqrt{2}\pi}\frac{(1-\nu)r_0}{Q(1-\nu-2\nu^2)}\frac{N}{\zeta(N+1)} = \tau\frac{N}{\zeta(N+1)}, \tag{10}$$

such that

$$\tau = \frac{9}{\sqrt{2}\pi}\frac{(1-\nu)r_0}{Q(1-\nu-2\nu^2)}, \tag{11}$$

and

$$H^* \sim \frac{1}{(1+1/N)}. \tag{12}$$

Equation (10) is a key result of this analysis and provides important insights into the physics of the size effect problem. Notably, the critical size is a function only of the shape of the material law (incorporated in N), the geometry of the specimen (incorporated in r_0, ζ, and Q), and the loading condition. Specifically, it is not a function of the specifics of the material's failure strength and extensibility.

We can determine the parameter τ by means of linear elastic fracture mechanics. Using Eq. (11) with the simulation parameters given in Sec. II, $Q = F^2$ (analytical expression for linear elastic fracture mechanics given in [25]), and $\nu = 1/3$, we find that $0.38r_0 \leqslant \tau_{\mathrm{LEFM}} \leqslant 2.21r_0$.

A comparison with the simulation results yields $\tau_{\mathrm{Sim}} = 0.65a_0 \approx a_0/\sqrt{2} = r_0$ (solid lines in Fig. 3), in good agreement with the linear elastic fracture analysis. Hence,

$$H^* \sim \frac{r_0}{(1+1/N)}. \tag{13}$$

This value also agrees with the prediction of quantized fracture mechanics that accounts for the discrete nature of the problem [34]. In the linear elastic case $N = 1$, Eq. (10) yields τ as fracture quantum, a characteristic system or material size (for crystals on the order of the lattice size or the bond spacing, i.e., $q = \mathcal{O}(r_0,a_0)$, or for granular materials on the order of the grain size, etc.).

From the scaling law in Eq. (12) it can also be concluded that the maximum critical size is achieved at the asymptotic limit $N \to \infty$. A strongly stiffening power-law material constitutive behavior can thus increase the critical size H^* by a multiple, assuming a constant crack ratio ζ, and in comparison to a softening behavior ($N \ll 1$) as seen in many engineering materials like metals (for instance, many metals could be modeled by a softening behavior, $N = 0.05$–0.5). Our analysis confirms the prediction made in Eq. (13), in which a strain softening will severely reduce the critical size H^*.

V. GENERALIZATION TO FIBROUS BIOMATERIALS

Many materials display a complex behavior and cannot be modeled with a one-parameter power law as given by Eq. (2). As a general representation, we propose a power-law series of the form

$$\Phi(r) = k_0 r_0 \varepsilon^* \sum_i \frac{a_i}{(N_i+1)}\left[\frac{\varepsilon(r)}{\varepsilon^*}\right]^{N_i+1}. \tag{14}$$

With the results of Sec. IV the critical size of a material with complex constitutive behavior reads as

$$H^* = \frac{9}{\sqrt{2}\pi}\sum_i \frac{a_i(1-\nu)r_0}{Q(1-\nu-2\nu^2)}\frac{N_i}{\zeta(N_i+1)} = \frac{\tau}{\zeta}\sum_i a_i\frac{N_i}{(N_i+1)}. \tag{15}$$

TABLE I. Coefficients a_i of the power-law potential series for MaSp1 spider silk dragline material.

N_i	0.1	0.6	10
$a_{i,\mathrm{MaSp1}}$	0.002679	0.229	0.7666

A prominent and well-studied example of a biomaterial that cannot be modeled by one parameter is spider dragline silk. The molecular structure and mechanical performance has been recently elucidated by molecular dynamics, as reported in [35]. Based on the results for the stress-strain behavior of MaSp1 dragline silk obtained from an atomistic simulation of a silk protein repeat, we derive a least-squares fit for the power-law series with positive coefficients. The only nonvanishing terms are $N_i = 0.1, 0.6, 10.0$. The series coefficients a_i are shown in Table I and the fit is shown in Fig. 4(a).

We note that r_0 is a length scale related to the dominating substructure of the material, e.g., the grain size or in the case of spider silk the size of the crystalline unit cell. In this analysis we set $r_0 \approx 10$ nm. It is reasonable to use the determined parameter $\tau = r_0$, although σ^* is approximately 1400 MPa and ε^* is approximately 62%, as the results for τ are independent of the actual strength [Eq. (10)]. The results for the critical size H^*_{MaSp1} are shown in Table II and agree remarkably well with experimental observations in the range of 20−150 nm [36,37].

Table III lists various fibrous biomaterials as well as their respective parameters N, which are then used to approximate their critical size H^* using Eq. (10) for $\zeta = 0.5$–0.15 and $r_0 = 10$ nm. It is notable that materials with a more pronounced stiffening behavior also seem to exhibit larger fibril diameters, as shown in Fig. 4(b), in support of the hypothesis put forth in our study. An exception is egg sack silk produced by the *B. mori* larva. This type of silk has an intrinsic softening behavior ($N = 0.3$–0.5) and displays fibril diameters of 8–100 nm [38]. This is clearly underestimated by our model, which predicts a critical size of only a few nanometers. As a protective hull, this type of silk is designed to absorb a large amount of energy and the cocoon design is highly redundant, such that a strain softening may be advantageous for this case. In contrast, dragline silk or elastin need to be resilient but also highly reliable, e.g., one dragline silk fiber has to carry the weight of a spider. Therefore, a robust and reliable design of the fibrils in the fibers is of higher importance.

We emphasize that the knowledge of the characteristic structural length scale r_0 is crucial. Therefore, while providing insights into potential trends, the compilation of data reported in Table III is only a rough estimate. For example, polycaprolactone fibers (PCL) display crystallite sizes of almost 10 nm, such that r_0 is likely larger than 10 nm. In that case, H^* increases in accordance with the observed fibril sizes in the fiber of 10–100 nm. Larger characteristic structural length scales have also been identified in biomaterials such as spectrin, where $r_0 \approx 75$ nm [39].

TABLE II. Flaw tolerance length scale in spider dragline silk MaSp1 for various crack size ratios ζ.

ζ	0.5	0.25	0.15	0.075
H^*_{MaSp1} (nm)	15.7	31.32	52.20	104.40

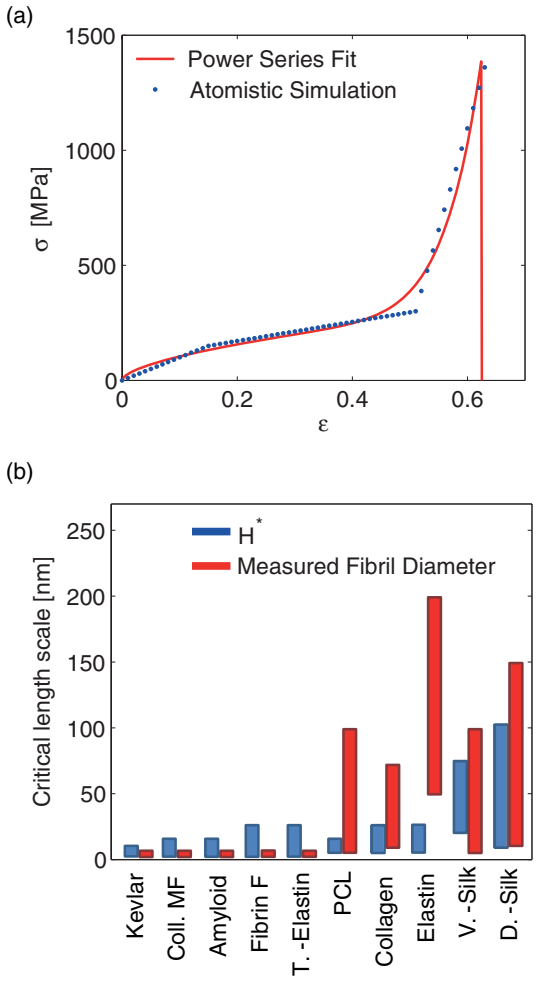

FIG. 4. (Color online) Power series fit to a biomaterial and comparison of the critical size to fibrous biomaterials. (a) Power series fit of a more complex material behavior, here spider dragline silk MaSp1. The parameters of the series are presented in Table I and the resulting critical size H^* is 16–105 nm for $\zeta = 0.15$–0.5, in good agreement with the measured diameters of spider silk fibrils (20–150 nm). (b) Critical size determined in this study (blue [left] bar), with a direct comparison to experimentally determined fibril diameters (red [right] bar) arranged in the order of increasing stiffness (from left to right). Confirming our hypothesis, materials with more pronounced stiffening behavior tend to have larger fibrils in agreement with the trend of the critical size.

VI. DISCUSSION AND CONCLUSION

Our analysis suggests that a material's nonlinear stiffening behavior is a generic strategy that enhances a structure's flaw tolerance. Indeed, many biopolymers show a universal stiffening behavior, caused by mechanisms such as backbone stretching after molecular unfolding or even network reorganization. The path to failure determines whether or not such a behavior is beneficial to the flaw tolerance mechanism.

TABLE III. Stiffness parameter N for various materials, the critical size H^* determined in this study and comparison to experimentally determined fibril diameter, H_{expt}.

Polymer material	N	$H^*_{15\%-50\%}$ (nm)	H_{expt} (nm)
Kevlar microfibrils[a]	1	4–20	~3.5
Collagen microfibrils[b]	1–2	4–30	~1.5
β-Amyloid[c]	1–2	4–30	3–5
Fibrin fibrils[d]	1–2	4–30	~4.5
Tropoelastin microfibrils[e]	1–5	4–50	~5
PCL[f]	2	10–30	10–100
Collagen fibrils[g]	2–3	10–50	20–70
Elastin[h]	2–5	10–50	50–200
Viscid silk[i]	7	40–75	10–100
MaSp1 dragline silk[j]	0.1, 0.6, 10.0	16–105	20–150

[a]Reference [47].
[b]Reference [48].
[c]Reference [49].
[d]Reference [50].
[e]Reference [51].
[f]Reference [52].
[g]References [48,53].
[h]Reference [54].
[i]References [2,55].
[j]References [36,37].

This leads to a trade-off between tangent stiffness and surface energy, since $H^* \sim \gamma_s E'$.

It has been shown that it is possible to chemically engineer polymeric materials with varying stiffening behavior, which may enable the implementation and experimental testing of the concepts put forth here [40–43]. An additional effect contributes to the observed behavior depicted in Fig. 3. A low initial stiffness, as induced by higher power-law exponents $N \gg 1$, increases the crack tip blunting throughout the deformation history and thus decreases the localization of stress [44]. This process cannot take place in materials with high initial stiffness. Furthermore, the size of the fracture process zone has been generally derived to scale with $\sim G_C E'$ [44]. Equation (5) predicts the same scaling law for H^*.

Flaw tolerance has been quantified in earlier studies to be a powerful mechanism to maintain a material's functionality from the nanoscale up [15,23,45]. A recent study provides evidence that the nonlinear stiffening behavior of a silk fiber increases the robustness of the spider web [46]. A loaded spider web structure localizes the web damage in only a few fibers. On a smaller scale, the derived scaling law $H^* \sim 1/(1 + 1/N)$ indicates that stiffening silk fibers consisting of nanoconfined fibrils of 20–150 nm (e.g., in dragline silk) are capable of maintaining their full strength despite possible flaws in the fiber material, as outlined in this paper. By controlling E' and γ_s at the scale of molecular bonds, the translation of nanoscale mechanical features to larger scales is enabled and leads to a synergistic interplay of effects at different length scales.

ACKNOWLEDGMENTS

This work was primarily supported by ONR-PECASE (Award No. N000141010562) and the German National Academic Foundation (Studienstiftung des deutschen Volkes). N.M.P. is supported by the European Research Council under the European Union's Seventh Framework Programme (FP7/2007-2013)/ERC Grant Agreement No. 279985 (Ideas Starting Grant BIHSNAM, 2012-2016). N.M.P. and M.J.B. acknowledge the support from the MIT-Italy program MITOR.

[1] P. Fratzl and R. Weinkamer, Prog. Mater. Sci. **52**, 1263 (2007).
[2] J. Gosline, M. Lillie, E. Carrington, P. Guerette, C. Ortlepp, and K. Savage, Philos. Trans. R. Soc. B **357**, 121 (2002).
[3] M. Y. Li, M. J. Mondrinos, M. R. Gandhi, F. K. Ko, A. S. Weiss, and P. I. Lelkes, Biomaterials **26**, 5999 (2005).
[4] E. Gentleman, A. N. Lay, D. A. Dickerson, E. A. Nauman, G. A. Livesay, and K. C. Dee, Biomaterials **24**, 3805 (2003).
[5] E. P. S. Tan, S. Y. Ng, and C. T. Lim, Biomaterials **26**, 1453 (2005).
[6] P. A. Janmey, Curr. Opin. Cell Biol. **3**, 4 (1991).
[7] M. Denny, J. Exp. Biol. **65**, 483 (1976).
[8] A. A. Griffith, Philos. Trans. R. Soc. A **221**, 163 (1921).
[9] Z. P. Bazant, J. Eng. Mech. Div., Am. Soc. Civ. Eng. **110**, 518 (1984).
[10] J. Mazars, G. Pijaudiercabot, and C. Saouridis, Int. J. Fract. **51**, 159 (1991).
[11] M. R. Wisnom, Compos. Sci. Technol. **59**, 1937 (1999).
[12] Z. P. Bazant, *Scaling of Structural Strength* (Taylor & Francis, New York, 2002).
[13] Z. P. Bazant, Proc. Natl. Acad. Sci. USA **101**, 13400 (2004).
[14] N. M. Pugno, Int. J. Fract. **141**, 313 (2006).
[15] H. J. Gao, B. H. Ji, I. L. Jager, E. Arzt, and P. Fratzl, Proc. Natl. Acad. Sci. USA **100**, 5597 (2003).
[16] H. J. Gao and S. H. Chen, J. Appl. Mech. **72**, 732 (2005).
[17] T. Giesa, M. Arslan, N. M. Pugno, and M. J. Buehler, Nano Lett. **11**, 5038 (2011).
[18] D. S. Dugdale, J. Mech. Phys. Solids **8**, 100 (1960).
[19] S. Kumar, M. A. Haque, and H. Gao, Appl. Phys. Lett. **94**, 253104 (2009).
[20] W. A. Curtin and H. Scher, J. Mater. Res. **5**, 554 (1990).
[21] C. S. Chang, T. K. Wang, L. J. Sluys, and J. G. M. van Mier, Eng. Fract. Mech. **69**, 1941 (2002).
[22] H. J. Gao and B. H. Ji, Eng. Fract. Mech. **70**, 1777 (2003).
[23] M. J. Buehler, H. M. Yao, H. J. Gao, and B. H. Ji, Modell. Simul. Mater. Sci. Eng. **14**, 799 (2006).
[24] T. Ackbarow, D. Sen, C. Thaulow, and M. J. Buehler, PLoS One **4**, e6015 (2009).
[25] H. Tada, P. C. Paris, and G. R. Irwin, *The Stress Analysis of Cracks Handbook*, 3rd ed. (ASME Press, New York, 2000).
[26] J. R. Rice and G. F. Rosengren, J. Mech. Phys. Solids **16**, 1 (1968).
[27] K. Hayashi, J. Mech. Phys. Solids **27**, 163 (1979).
[28] J. Pan, J. Mech. Phys. Solids **34**, 617 (1986).

[29] S. Plimpton, J. Comput. Phys. **117**, 1 (1995).
[30] K. Kremer and G. S. Grest, J. Chem. Phys. **92**, 5057 (1990).
[31] G. H. Altman, F. Diaz, C. Jakuba, T. Calabro, R. L. Horan, J. S. Chen, H. Lu, J. Richmond, and D. L. Kaplan, Biomaterials **24**, 401 (2003).
[32] M. S. Daw and M. I. Baskes, Phys. Rev. B **29**, 6443 (1984).
[33] M. J. Buehler, *Atomistic Modeling of Materials Failure* (Springer, New York, 2008).
[34] N. M. Pugno and R. S. Ruoff, Philos. Mag. **84**, 2829 (2004).
[35] S. Keten and M. J. Buehler, J. R. Soc. Interface **7**, 1709 (2010).
[36] S. Keten and M. J. Buehler, Appl. Phys. Lett. **96**, 153701 (2010).
[37] N. Du, Z. Yang, X. Y. Liu, Y. Li, and H. Y. Xu, Adv. Funct. Mater. **21**, 772 (2011).
[38] I. Greving, M. Z. Cai, F. Vollrath, and H. C. Schniepp, Biomacromolecules **13**, 676 (2012).
[39] T. J. Byers and D. Branton, Proc. Natl. Acad. Sci. USA **82**, 6153 (1985).
[40] K. C. F. Leung, P. M. Mendes, S. N. Magonov, B. H. Northrop, S. Kim, K. Patel, A. H. Flood, H. R. Tseng, and J. F. Stoddart, J. Am. Chem. Soc. **128**, 10707 (2006).
[41] K. A. Erk, K. J. Henderson, and K. R. Shull, Biomacromolecules **11**, 1358 (2010).
[42] C. P. Broedersz and F. C. MacKintosh, Soft Matter **7**, 3186 (2011).
[43] J. R. Capadona, K. Shanmuganathan, D. J. Tyler, S. J. Rowan, and C. Weder, Science **319**, 1370 (2008).
[44] T. L. Anderson, *Fracture Mechanics: Fundamentals and Applications,* 3rd ed. (Taylor & Francis, Boca Raton, FL, 2005).
[45] B. H. Ji and H. J. Gao, J. Mech. Phys. Solids **52**, 1963 (2004).
[46] S. W. Cranford, A. Tarakanova, N. Pugno, and M. J. Buehler, Nature **482**, 72 (2012).
[47] L. C. Sawyer, R. T. Chen, M. G. Jamieson, I. H. Musselman, and P. E. Russell, J. Mater. Sci. **28**, 225 (1993).
[48] A. Gautieri, S. Vesentini, A. Redaelli, and M. J. Buehler, Nano Lett. **11**, 757 (2011).
[49] R. Paparcone and M. J. Buehler, Biomaterials **32**, 3367 (2011).
[50] M. Guthold, W. Liu, E. A. Sparks, L. M. Jawerth, L. Peng, M. Falvo, R. Superfine, R. R. Hantgan, and S. T. Lord, Cell Biochem. Biophys. **49**, 165 (2007).
[51] C. Baldock, A. F. Oberhauser, L. A. Ma, D. Lammie, V. Siegler, S. M. Mithieux, Y. D. Tu, J. Y. H. Chow, F. Suleman, M. Malfois, S. Rogers, L. A. Guo, T. C. Irving, T. J. Wess, and A. S. Weiss, Proc. Natl. Acad. Sci. USA **108**, 4322 (2011).
[52] M. Mochizuki, M. Hirano, Y. Kanmuri, K. Kudo, and Y. Tokiwa, J. Appl. Polym. Sci. **55**, 289 (1995).
[53] A. Masic, L. Bertinetti, R. Schuetz, L. Galvis, N. Timofeeva, J. W. C. Dunlop, J. Seto, M. A. Hartmann, and P. Fratzl, Biomacromolecules **12**, 3989 (2011).
[54] M. A. Lillie and J. M. Gosline, Int. J. Biol. Macromol. **30**, 119 (2002).
[55] T. A. Blackledge and C. Y. Hayashi, J. Exp. Biol. **209**, 3131 (2006).